scientific reports

OPEN

Origin of the solar-cycle imprint on global sea level change

Shuhei Masuda[1]✉, John Philip Matthews[2,3] & Yosuke Alexandre Yamashiki[4]

In order to improve insight into the causes of sea-level variability we investigate poorly understood 11-year solar-cyclic oscillations in the temporal rate of global sea-level change. Our approach is based mainly on a thorough reassessment of relevant historical datasets and on an analysis of precise altimetric sea-height observations. We first demonstrate that the temporal rates of change of water volumes stored on land also fluctuate on comparable 11-year timescales, suggesting that the solar-cyclic sea level oscillations we observe result from adjustments taking place in the water-mass balance between the oceanic and terrestrial realms. We then show that these water-mass transfers result primarily from systematic changes that take place in the El Niño Southern Oscillation during the course of the solar cycle. We interpret these evolutionary changes on the basis of a causal sequence that commences within the Quasi-Biennial-Oscillation, a system of regular upper-atmospheric wind reversals that exhibits a clear solar-cyclic dependence and has a well-defined impact on the development of the Madden Julian Oscillation. The latter can influence the strength and rate of evolution of the El Niño Southern Oscillation which, in turn, determines the level of net terrestrial water storage through its effect on rainfall patterns. Recognition of this underlying solar-cyclic modulation advances our understanding of the factors determining historical and future variability in global mean sea level.

With roughly 10% of the world's population living in low-lying (< 10 m above sea level) coastal zones[1], increases in global mean sea level (GMSL) inevitably engender widespread societal anxiety and reinforce the need for accurate sea-level prediction[2,3]. It is therefore of particular concern that GMSL has been rising monotonically over the last 100 years (Fig. 1 grey line)[4,5].

GMSL is determined primarily by contributions from steric height change (ocean expansion on warming), meltwater runoff (from glaciers), ice losses from Greenland and Antarctica, and changes in terrestrial water storage (TWS), which, roughly speaking, is determined by the difference between terrestrial precipitation and river runoff. Sea-level height measurements made by satellite altimeters (from 1993 onwards) have enabled the magnitudes of these separate contributions to be accurately assessed[5–7]. Thus from 1993 to 2018, the average rate of sea level rise of 3.16 mm/year consisted of 1.19 mm/year from thermal expansion of the subsurface ocean due to global warming and 1.97 mm/year from barystatic oceanic mass increase (mostly through the melting of polar ice).

In addition to this well-defined linear trend, long-term coastal tide-gauge observations have revealed quasi-decadal variability in the temporal rate of change of global mean sea level ($GMSL_T$) of between 3 and 5 mm/year in amplitude[8,9], which has been linked[9] to the 11-year solar cycle (supplementary text #1). In Fig. 1 (red line) we use longer-term reconstruction data to confirm the presence of essentially similar oscillations. The close correlation of these signals with solar activity (as represented by the sunspot number, SSN; blue line) is quantified by a statistical significance of over 80% (correlation coefficient = 0.12 with 115 degrees of freedom), although we note the presence of a number of anomalous peaks in the time series (which are discussed later). In contrast to $GMSL_T$, we note that the corresponding GMSL-SSN relation is difficult to isolate or identify since it is buried in a large monotonically increasing trend.

These clear indications of solar influence have received no generally accepted interpretation. A putative origin within the thermal expansions and contractions of oceanic waters in response to the cyclic variations in Total Solar Irradiance (TSI) can be rejected, as this would require some 5 to 7 times more variability in heat input than is actually observed within the TSI cycle itself[9]. An alternative interpretation relies on solar-wind modulation of the incoming galactic cosmic ray (GCR) flux to produce an amplification of the variability of the radiative flux entering the ocean by influencing basin-wide cloud coverage[10,11]. However, recent oceanographic

[1]Research Institute for Global Change, Japan Agency for Marine-Earth Science and Technology (JAMSTEC), 2-15 Natsushima-cho, Yokosuka 237-0061, Japan. [2]Environmental Satellite Applications, Llys Awel, Mount Street, Menai Bridge, Anglesey LL595BW, UK. [3]Institute of Liberal Arts and Sciences, Kyoto University, Kyoto 606-8501, Japan. [4]Graduate School of Advanced Integrated Studies in Human Survivability, Kyoto University, Yoshida-Nakaadachicho 1, Sakyo-ku, Kyoto 606-8306, Japan. ✉email: smasuda@jamstec.go.jp

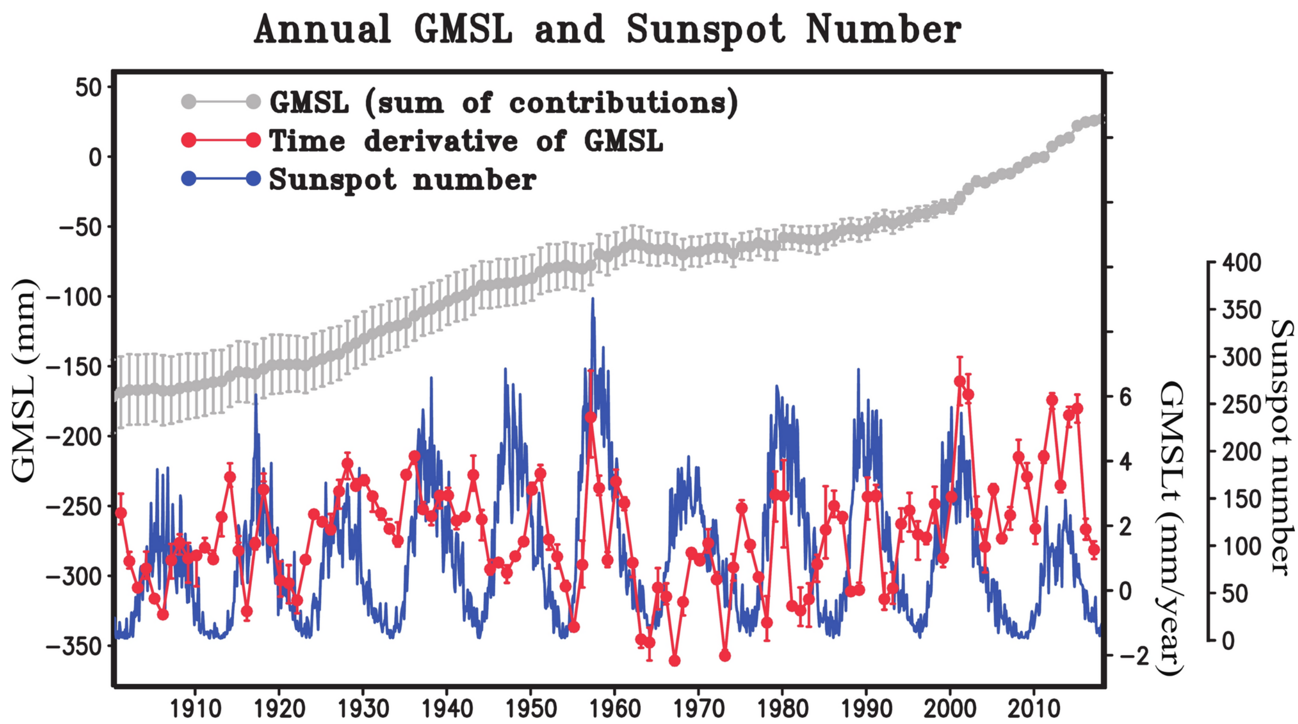

Fig. 1. Global mean sea level and its temporal change rate. Annual Global Mean Sea Level (sum of major contributions; grey curve) after 1900 compiled from a range of available data as provided by Frederikse et al.[5]. Error bars denote 90% confidence intervals. The sea-level change rate derived from these same data ($GMSL_T$) is shown in red. Sunspot numbers are given in blue.

data indicate that the contribution from oceanic thermal expansion exhibits little relation to solar-cycle phase. This latter result is consistent with the conclusions of[9] and of other ocean-state estimations[12] (supplementary text #2 and Fig. S1).

Results

Based on an in-depth consideration of global freshwater circulation, historical records and recently acquired remotely-sensed observations of both sea level and terrestrial water distributions, we show that these sea level oscillations stem mainly from variability in TWS arising from changes in the water-mass balance between the oceanic and terrestrial realms. In order to demonstrate the causal effect of such water-mass redistributions, we first investigate the long-term record offered by the Palmer Drought Severity Index (PDSI)[13] which uses historical temperature and precipitation data to estimate relative dryness on the basis of a standardized index for terrestrial conditions that ranges from − 10 (dry) to + 10 (wet). Negative values of the time derivative ($PDSI_T$) indicate a net discharge of water from land to sea (corresponding to increasing GMSL i.e. positive values of $GMSL_T$) (see "Materials and Methods"). Results derived for $PDSI_T$ are given in Fig. 2A (red line) and show a clear 11-year periodicity which is highly correlated with the prevailing solar activity. The correlation between the red and blue curves is significant at a 99.9% level or higher (correlation coefficient = − 0.31 with 1174 degrees of freedom).

However, as the PDSI data contain a wide variety of influences (see supplementary text #3), the synchronization of $PDSI_T$ with the 11-year solar cycle breaks down occasionally (e.g., peaks in 1940s, 1960s and 1970s), as Fig. 2A and thus Fig. 1 both demonstrate. The histogram-style plot of Fig. 2B nevertheless shows the robust underlying dependence of $PDSI_T$ on the 11-year solar cycle that is a salient feature of these longer-term data. For SSN values above 100 (corresponding to solar maximum conditions; Smax), higher values of SSN correspond to more negative values of $PDSI_T$. Thus, for SSN = 100 we have $PDSI_T$ = 0.004 while for SSN = 280 then $PDSI_T$ = − 0.033. These more negative values of $PDSI_T$ generally correspond to larger $GMSL_T$ values. In contrast, during solar minimum (SSN ≦ 100; Smin), the values of $PDSI_T$ remain weakly positive centered roughly on $PDSI_T$ = 0.003 and are significantly larger than the values recorded under Smax conditions when $GMSL_T$ values are generally negative.

The relation between large-scale transfers of water from land to sea and mean sea level change, as indicated by this analysis of the long-term PDSI index, can be examined in a more quantitative fashion in order to better understand the underlying mechanisms. In Fig. 3 we use post-1993 altimetric data (green line) to accurately quantify $GMSL_T$ and to relate it to both terrestrial water storage and to the background variability in solar activity. It is clear that $GMSL_T$ follows the roughly sinusoidal variation in GCR count over the solar cycle (shown in blue), a result that is generally consistent with the post 1993 data presented in Fig. 1. In the case of Fig. 3 the (one

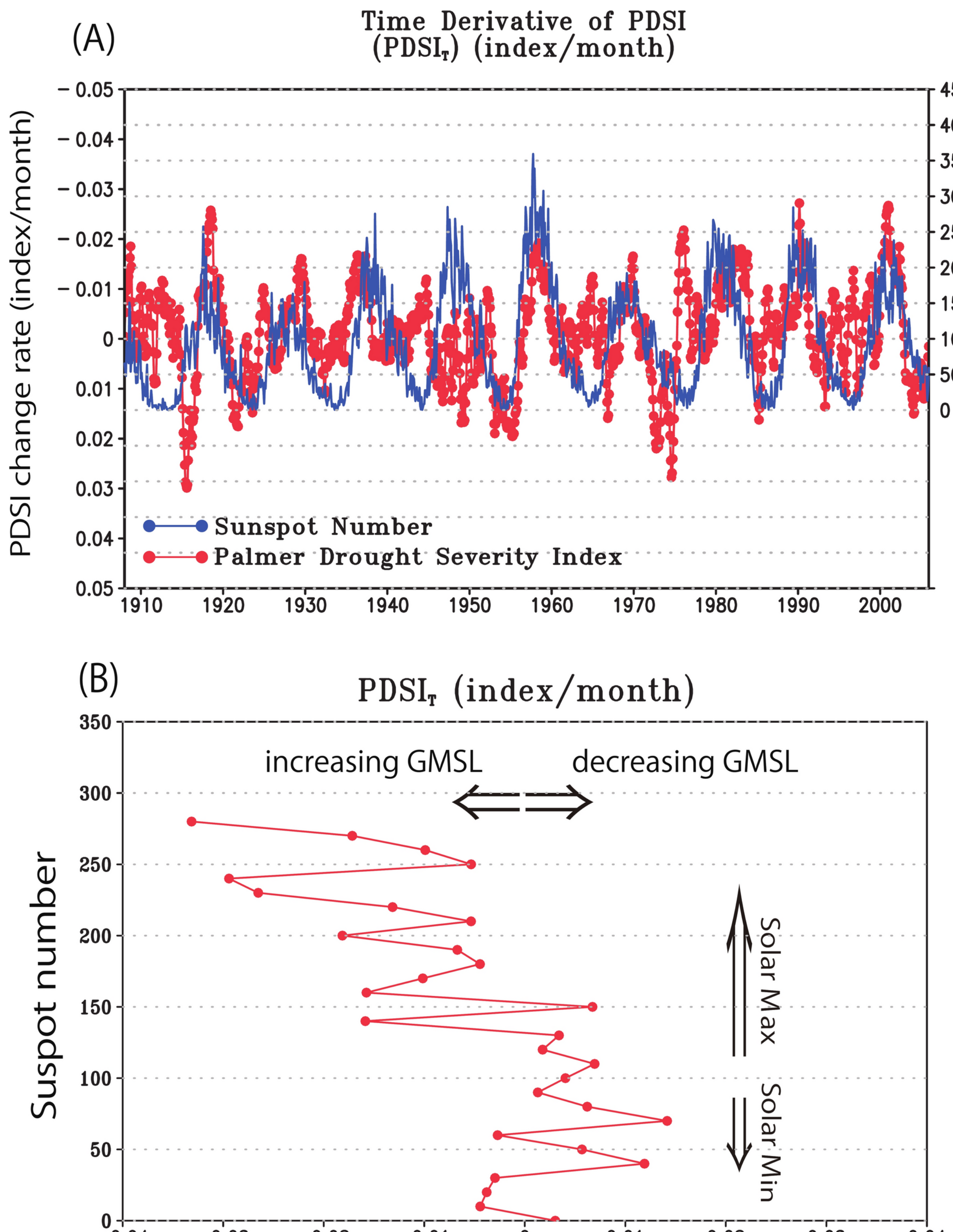

Fig. 2. Dependence of PDSI$_T$ on solar activity. (**A**) Comparison of global mean Palmer Drought Severity Index change-rates (PDSI$_T$) using a 3-year running mean (red curve) with sunspot number (SSN) (blue) for years 1908 to 2005. (**B**) PDSI$_T$ for each bin interval used to sort the SSN data (the bin intervals represent increments of 10). Mean values are calculated when the data number exceeds 5.

standard deviation) amplitude of the sinusoidal fluctuation in GMSL$_T$ lies at 1.33 mm/year (see supplementary text #4), a figure that we employ later.

In order to demonstrate the causal effect of large-scale water-mass redistributions on mean sea level, we next transform TWS storage data (expressed in units of gigatons; see "Materials and Methods" and ref.[14]) into

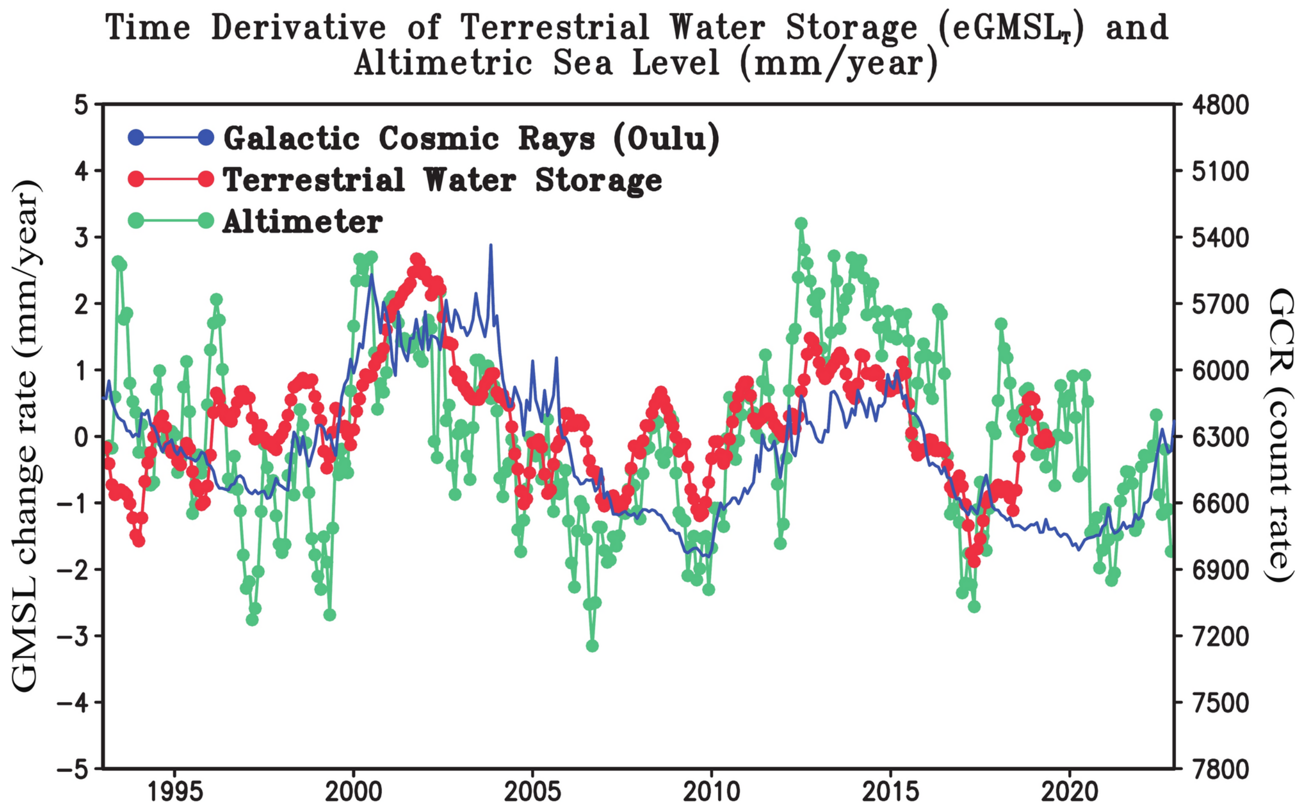

Fig. 3. Temporal change rate of the altimetric global mean sea level and its relation to solar and terrestrial variables. The de-trended global-mean monthly change-rate in sea level derived from altimeter data with seasonal variations removed (green curve). The contribution (eGMSL$_T$) from terrestrial water storage is shown in red. Both are processed using a 3-year running mean. Galactic Cosmic Ray count rates at Oulu are given in blue. The correlation between the green and red curves is significant at a 99.9% level or higher (correlation coefficient = 0.52 with 316 degrees of freedom). The correlation between the green and blue curves is also significant at a 99.9% level or higher (correlation coefficient = – 0.50 with 358 degrees of freedom).

"equivalent" GMSL values (denoted as eGMSL). To do this we perform a global summation of terrestrial water storage assessments (though excluding Greenland and Antarctica), and then divide the net result by the fresh water density of 1.0×10^6 g/m^3 and by the total area of the oceans of 3.6×10^{14} m^2. Note that positive values of the time derivative (eGMSL$_T$) indicate net discharge of water from land to sea and correspond to negative values of the time derivative of TWS (see "Materials and Methods"). The results derived for eGMSL$_T$ are given in Fig. 3 (red line). They also show sinusoidal variability but now with an amplitude near 0.86 mm/year (representing one standard deviation). The clear 11-year periodicity exhibited here is comparable in amplitude and phase to the oscillatory GMSL$_T$ signal present in the altimeter data (green line). This demonstrates that the 11-year solar-synchronized variation of GMSL$_T$ is mostly defined by change in TWS, as are the year-to-year variations of the GMSL budget[15] (see supplementary text #5).

Synoptic mapping of PDSI$_T$ can reveal the important global implications of the dynamical processes driving these water-mass redistributions. Thus the geographical distributions of PDSI$_T$ are provided in the composites of Fig. 4, corresponding to Smax (SSN > 100) and Smin (SSN ≦ 100), respectively. In Fig. 4A, the pattern of PDSI$_T$ for Smax indicates progressive drying in the Amazon basin, Australia, South Africa, India and South-East Asia including the maritime continents. These trends point to reduced terrestrial water storage and so increasing GMSL. In contrast, the changes towards wetter conditions taking place in southern North America, Central Asia and southern China will tend to decrease GMSL. In terms of the total budget, the former effect outweighs the latter, which results in an increase in GMSL during the Smax phase. It is particularly noticeable that the geographical pattern exhibited in Fig. 4A is similar to that derived from empirical orthogonal function (EOF) analysis shown by Dai et al.[16], which they linked to El Niño Southern Oscillation (ENSO) activity.

The pattern for Smax conditions exhibited in Fig. 4A is largely reversed for Smin conditions, as shown in Fig. 4B. In this case the Smin distribution is rather similar to La Niña conditions (Fig. 4B), particularly in terms of wet trends in the Amazon Basin and across eastern most of Australia. The total budget points to a decrease in GMSL during the Smin phase (Fig. 2B). Generally, the spatial patterns shown in Fig. 4A,B are consistent with results derived from TWS data (Fig. S2) although they cover a shorter time period. They are also consistent with the global ENSO-induced precipitation pattern discussed elsewhere[17]. Note that the total precipitation deposited per year over the oceans amounts to 3.91×10^5 km^3 [18], while the observed 11-year oscillation in GMSL$_T$ (of amplitude 1.35 mm/year) corresponds to variability in only about 0.12% (4.9×10^2 km^3/year) of this total. Thus,

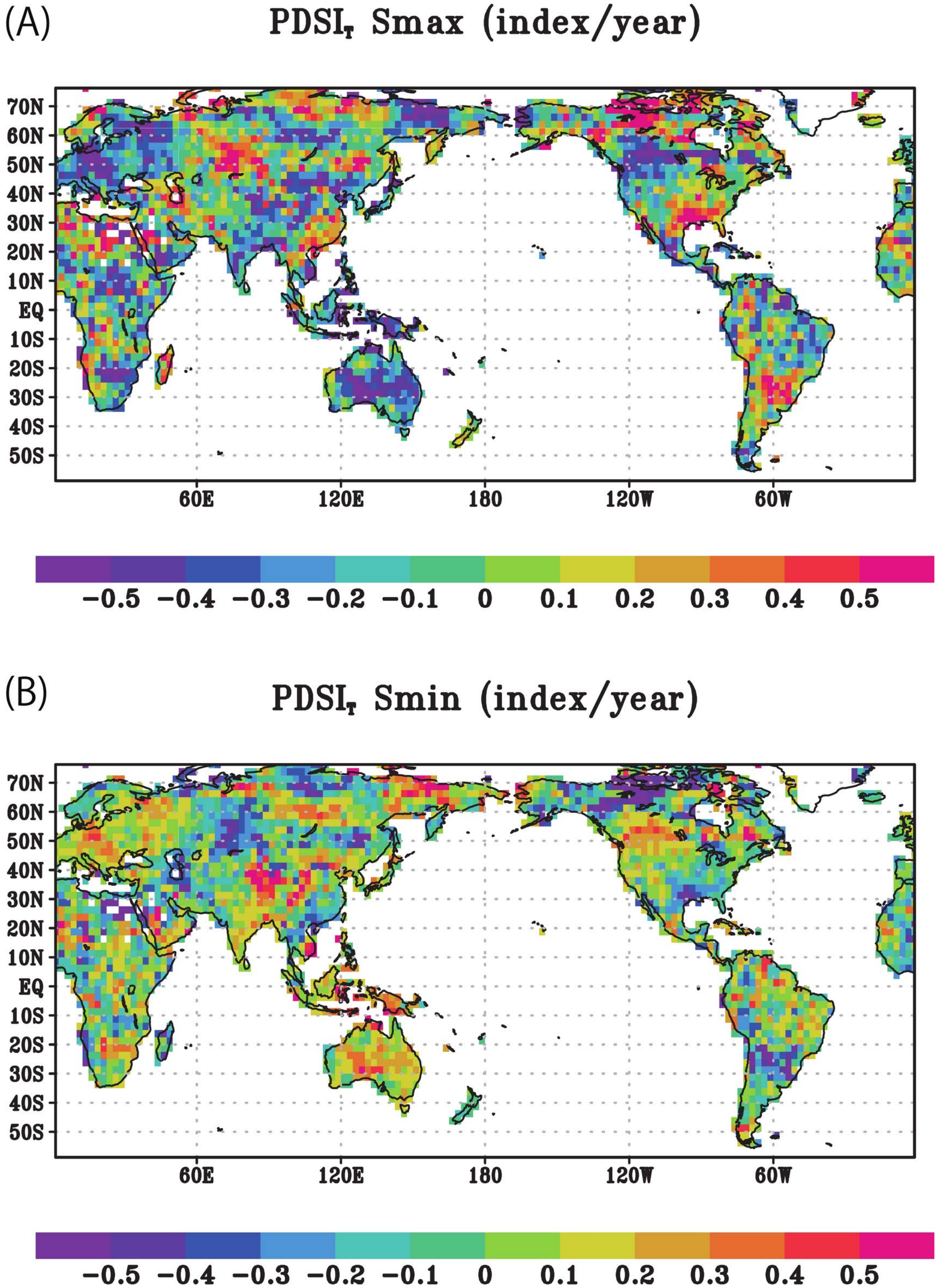

Fig. 4. Geographical distribution of PDSI$_T$ composited by SSN. (A) Composite values of PDSI$_T$ under solar maximum conditions (SSN > 100) and (B) under solar minimum conditions (SSN $\leqq$ 100) for years 1908 to 2005.

relatively minor fluctuations in the global water cycle can generate the levels of sea level change under discussion here.

Overall, these results suggest that the 11-year solar cycle can modulate precipitation and associated terrestrial water-mass redistributions by altering the genesis and climatological impact of the ENSO. We note that in the specific case of the Amazon, earlier research has indicated a link between Amazon runoff during the twentieth century and the 11-year solar cycle[19,20], with more recent evidence further supporting this suggestion[21]. Such a link is qualitatively consistent with our results, assuming that riverine discharge is largely reflective of basin-wide water storage levels. That is, high rainfall in the Amazon basin increases both instantaneous river discharge and the basin-wide water storage remaining on land, while the net contribution is towards a lowering of global sea level.

We next examine our earlier suggestion that the genesis and climatological impact of the ENSO can be influenced by solar activity. Figure 5A shows absolute values of the temporal variability of the averaged sea surface temperature in the NINO3.4 region (5°N–5°S and 170°–120°W), which is a useful index for classifying ENSO conditions. In particular, the absolute value of the temperature change-rate, $|NINO_T|$, provides a good overall indication of the level of activity or rapidity of development of a given El Niño or La Niña event. In Fig. 5A the modulus $|NINO_T|$ is represented by a blue line, while the SSN time series is shown in red. Since ENSO genesis is known to depend on various factors such as subsurface conditions in the tropical ocean, meso-scale atmospheric/oceanic dynamics, and air-sea interactions in terms of heat, fresh water and momentum, individual ENSO events can develop in highly diverse ways. Nevertheless, certain general characteristics become apparent over decadal time scales.

In parallel with the high variability shown in Fig. 5A, the time series of $|NINO_T|$ also reveals a subtle tendency for surface temperature change rate**s** to increase during periods of Smin and to subside during periods of Smax. This synchronization with solar activity is clearly revealed by the wavelet analysis presented in Fig. 5B, in which the wavelet amplitudes of the $|NINO_T|$ time series show large values as they overlap with the strong band of wavelet amplitudes (white contours) centered on 11 years (132 months) that are derived from the SSN time series. The relation is best defined within the approximate periods from 1870–1890, 1940–1960, 1975–1985 and, with poorer definition, around 2005. The appearance of large amplitude spots from 1940–2000 shows that more active solar conditions (Solar Cycles 17 to 23) were generally prevalent during this period. We note that the amplitudes of the 11-year related signals are comparable to those of the interannual variability (<60 months), where the most energetic frequency bands of ENSO activity are located. This indicates that the synchronized variations exhibited in Fig. 5B, which can be viewed as a solar-cyclic imprint on the $|NINO_T|$ time series, represent an important source of ENSO modulation. It should also be noted that it is difficult to unmask this relation by simply studying the time variation of the ENSO parameter $NINO_T$ (now treated as a real number) in relation to SSN, as Fig. S3 demonstrates.

Our explanation of this ENSO modulation by solar activity relies firstly on a consideration of the Quasi-Biennial Oscillation (QBO), which is an upper atmospheric wind-reversal phenomenon of key importance within the climate system and one that is strongly influenced by solar activity[22–25]. Recently Hood et al. (2023) found firm evidence that both the QBO and solar activity can influence the Tropical Madden–Julian Oscillation (MJO)[26], with MJO amplitudes significantly larger under solar minimum conditions when the QBO phase is easterly. In turn, the MJO is known to influence both phases of ENSO genesis (i.e. positive and negative), for example through the occurrence of westerly and easterly wind bursts in the tropical Pacific Ocean that may potentially initiate El Niño or La Niña activity[27–29].

By making use of these recent research advances, we can investigate the extent to which the relationship between $NINO_T$ and solar activity (as defined by the GCR flux) depends on the phase of the QBO and the sign of the $NINO_T$ parameter. For the QBO we have adopted a commonly-used definition for the westerly and easterly phases as periods when the westerly and easterly wind speeds at the 50 hPa level exceed 5 and 10 m/s respectively.

As shown in Fig. 6A, the overall dependence on solar activity is not as clearly defined as in Fig. 5. In terms of the frequency of occurrence, for values of $NINO_T > 0.6$ (i.e. to the right of the grey line that roughly demarcates the major El Niño events), 14 events occur during Smax and 23 during Smin. In terms of magnitude, the ranges of values taken are similar while the maximum values are 0.88 and 0.96 respectively. When this is divided into subsets according to QBO phase, the frequency of occurrence for the QBO westerly phase (cyan) is 12 events during Smax and 16 during Smin (1.3 times greater), while for the QBO easterly phase (magenta) the frequency is 2 and 7, respectively, with a larger ratio (3.5 times). The maximum values are 0.88 (Smax) and 0.96 (Smin; difference 0.08) for the QBO westerly phase and 0.72 and 0.87 (difference 0.15) for the QBO easterly phase. Thus the dependence on solar activity is somewhat better defined for the QBO easterly-phased values.

However, a stronger dependence is evident for periods when $NINO_T$ is negative (Fig. 6B). Analyzing in a similar fashion but now for $NINO_T < -0.6$ (roughly indicative of the major La Niña events), there are 8 events in total during Smax and 15 events during Smin. In terms of magnitude, the ranges of these events are more diverse, with minimum values of − 0.84 and − 1.10 respectively. Dividing as before into subsets based on QBO phase also reveals significant differences. The frequency of occurrence for the QBO westerly phase (cyan) is 5 during Smax and 8 during Smin (1.6 times), while the corresponding values are 3 and 7 for the QBO easterly phase (2.3 times). With regard to the minimum values (and bearing in mind the negative signs) we have − 0.84 (Smax) and − 0.68 (Smin; a difference of 0.08) for the QBO westerly-phased values, while the corresponding QBO easterly-phased values are − 0.73 (Smax) and − 1.10 (Smin; a difference of 0.37). This simple analysis reveals a more prominent solar influence for easterly QBO phases under solar minimum conditions, a result that closely parallels the requirements for enhanced MJO growth reported by Hood et al. (2023).

In terms of the relevant statistical parameters, when the correlation between $NINO_T$ and GCR is derived solely for the period when QBO phase is easterly, the correlation coefficient is − 0.21 when $NINO_T$ is negative and 0.16 when $NINO_T$ is positive. These values lie at 95% and 80% significance levels (with 110 and 81 degrees of freedom respectively). In contrast, no clear dependence is seen when the QBO phase is westerly (cyan). In this latter case the correlation coefficient is 0.07 when $NINO_T$ is negative and 0.09 when $NINO_T$ is positive. Neither of these values is significant (with 202 and 165 degrees of freedom respectively).

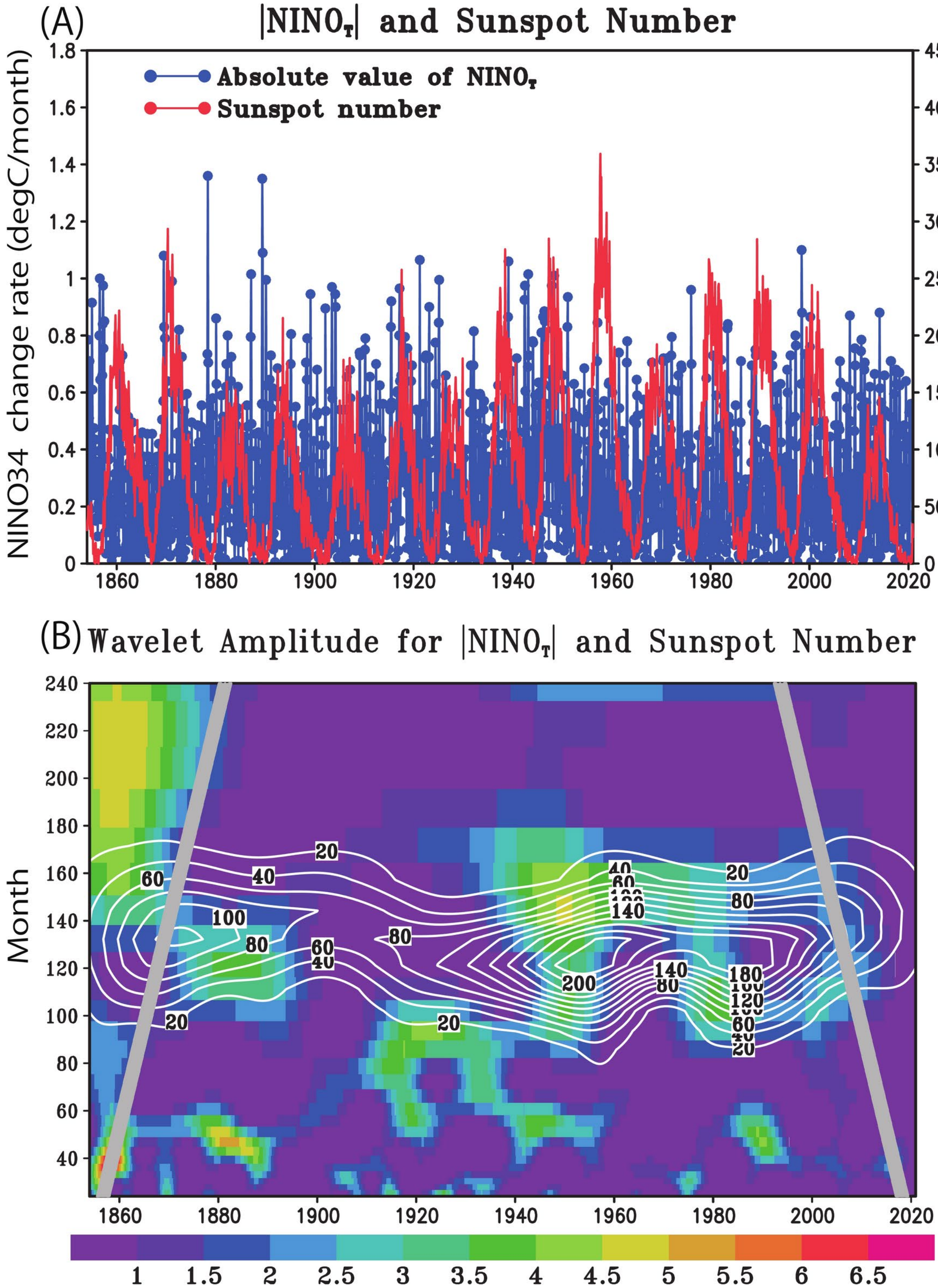

Fig. 5. Showing the modulation of NINO$_T$ at 132-month periodicity corresponding to the 11-year solar cycle. (**A**) The absolute value of NINO34 sea surface temperature change rate (|NINO$_T$|: blue curve) with sunspot number (SSN: red) for the period of 1854 to 2020. (**B**) The white contours represent the wavelet power spectrum for SSN, while shaded colors denote wavelet power spectrum for |NINO$_T$|. The grey lines define the cone of influence of the wavelet power spectrum.

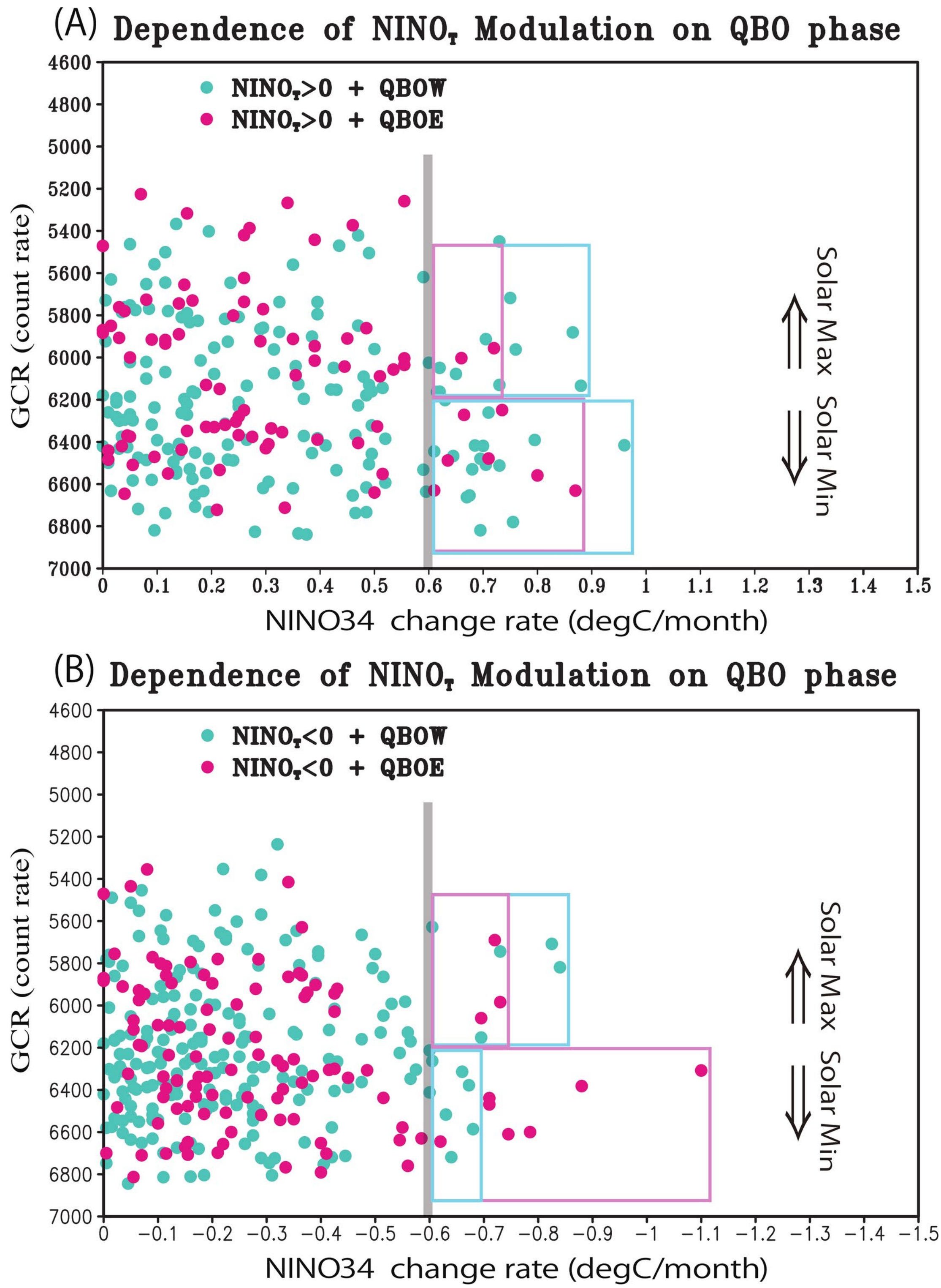

Fig. 6. Dependence of NINO$_T$ solar modulation on QBO phase. (**A**) Scatter plot of NINO34 sea surface temperature change rate (NINO$_T$) in relation to solar activity (GCR count rate) in the case of positive NINO$_T$, corresponding to the El Niño development phase for the period of 1965–2020. The cyan dots are for QBO westerly phase, while magenta dots represent easterly QBO phase. (**B**) The same as A but for the case of negative NINO$_T$, corresponding to the La Niña development phase. Significant dependence on solar activity is observed for magenta points in case (**B**), when the QBO phase is easterly and NINO$_T$ is negative.

Despite the relatively short data length used in our analysis (covering solar cycles 20 to 24), these results demonstrate a dependence of $NINO_T$ on solar activity and also provide a good indication of its relation to QBO phase. On the basis of these findings, we hypothesize that more energetic ENSO (especially La Niña) activity develops during periods when Smin and easterly QBO phase coincide, since then larger-amplitude MJO generation is more likely to take place. Although this stimulation has been observed in relation to several events[30], an in-depth treatment of the complex sequence of mechanisms involved in our interpretation lies outside the scope of the present article and will be the subject of future observational and modelling studies. We note, however, that the pioneering work of Labitzke and van Loon[22,31] laid the groundwork for such a comprehensive approach by reporting that certain atmospheric modes were stimulated under specific QBO phase conditions (see supplementary text #6).

The amplification of the MJO should influence key aspects of subsequent ENSO activity, with increases in the speed of El Niño and La Niña development indicated within the data of Fig. 6. The speed of ENSO development is closely related to the amplitude of the event, though the latter is not necessarily determinative, in part due to the variety of potentially unstable phenomena inherent in the tropical atmosphere and oceans. This behavior underlines the need to recognize the importance of time-differentiated physical quantities. In specific terms relevant to the present study, a more rapid evolution to strong La Niña conditions will lead to increases in the levels of precipitation falling over land[4] and thus have the effect of lowering global mean sea level when averaged over decadal time scales. Solar activity affects the MJO on an intra-seasonal time scale and ENSO affects precipitation with a lag of approximately 2 months[16], so the whole process can be seen as an intra-year variation (Fig. 7). Although we have found a statistically valid link between global sea level changes and solar activity, a connection that is effected through ENSO variability, the fact that $|NINO_T|$ is dependent on a range of other factors means that there are times when the anticipated relation breaks down, such as when the genesis and evolution of a large El Niño event depends solely on oceanic conditions so that the solar-cyclic influence becomes secondary or is wholly masked. Put another way, the link between MJOs and ENSOs contains uncertainty. This provides a general explanation of why some peaks in the plot of $GMSL_T$ versus sunspot number of Fig. 1 and in the $PDSI_T$ plot of Fig. 2A appear "out-of-phase".

Conclusion
In summary, this work considers the origin of an important aspect of the solar-cycle "footprint" on earth's climate that has been largely overlooked in previous analyses. It demonstrates that the sun's 11-year cycle modulates the rate of change of global mean sea level ($GMSL_T$) by inducing systematic changes in the water-mass balance between the oceanic and terrestrial realms (Fig. S4). Such variations in the land-sea partition of precipitation (and hence in TWS) reflect the evolution of rainfall patterns during the course of the solar cycle across regions influenced by the ENSO. Furthermore, our study has revealed an important determinative factor in sea level development by establishing that this solar-cyclic imprint on $GMSL_T$ is sensitive to QBO phase, specifically around solar minimum under easterly QBO conditions, as then induced MJO amplitudes are generally larger and thus the potential impact on ENSO development more pronounced. A firmer appreciation of the origin and impact of these aspects of underlying solar control, together with knowledge of local impacts[32,33], should contribute to improved projections of the future variability of sea level in coastal zones in addition to the local influences.

Materials and methods
Palmer Drought Severity Index
The Palmer Drought Severity Index (PDSI) is a climate index. It is calculated from temperature and precipitation data and is used to estimate relative terrestrial dryness. A soil–water balance model is assumed in the estimation process.

Terrestrial water storage data
We mainly use the reconstructed terrestrial water storage data[14] derived by assimilating satellite observations obtained as part of the Gravity Recovery and Climate Experiment (GRACE) mission. GRACE detects fluctuations in gravity by measuring the changes in distance and velocity between twin spacecraft as they orbit Earth and can thereby detect variability in terrestrial water storage with unprecedented accuracy. In order to exploit these data in an effective manner, historical near-real-time meteorological datasets have been used in parallel with ensemble runs of a dedicated statistical model. We used a reconstructed dataset utilizing the GRACE product which was generated with a meteorological forcing derived from the ERA5 dataset for 1979–2019, as this covers the most recent period amongst several reconstructed datasets. In terms of overlapping periods, other datasets show similar time derivatives, and thus our conclusions hold irrespective of the type of forcing used. Further details of these aspects are summarized in Humphrey and Gudmundsson[14].

Relation between changes in terrestrial water storage and global mean sea level
From a global perspective, changes in terrestrial water storage can be interpreted as having a direct effect on mean sea level, at least on the inter-annual time scales relevant to our study (fig. S4).

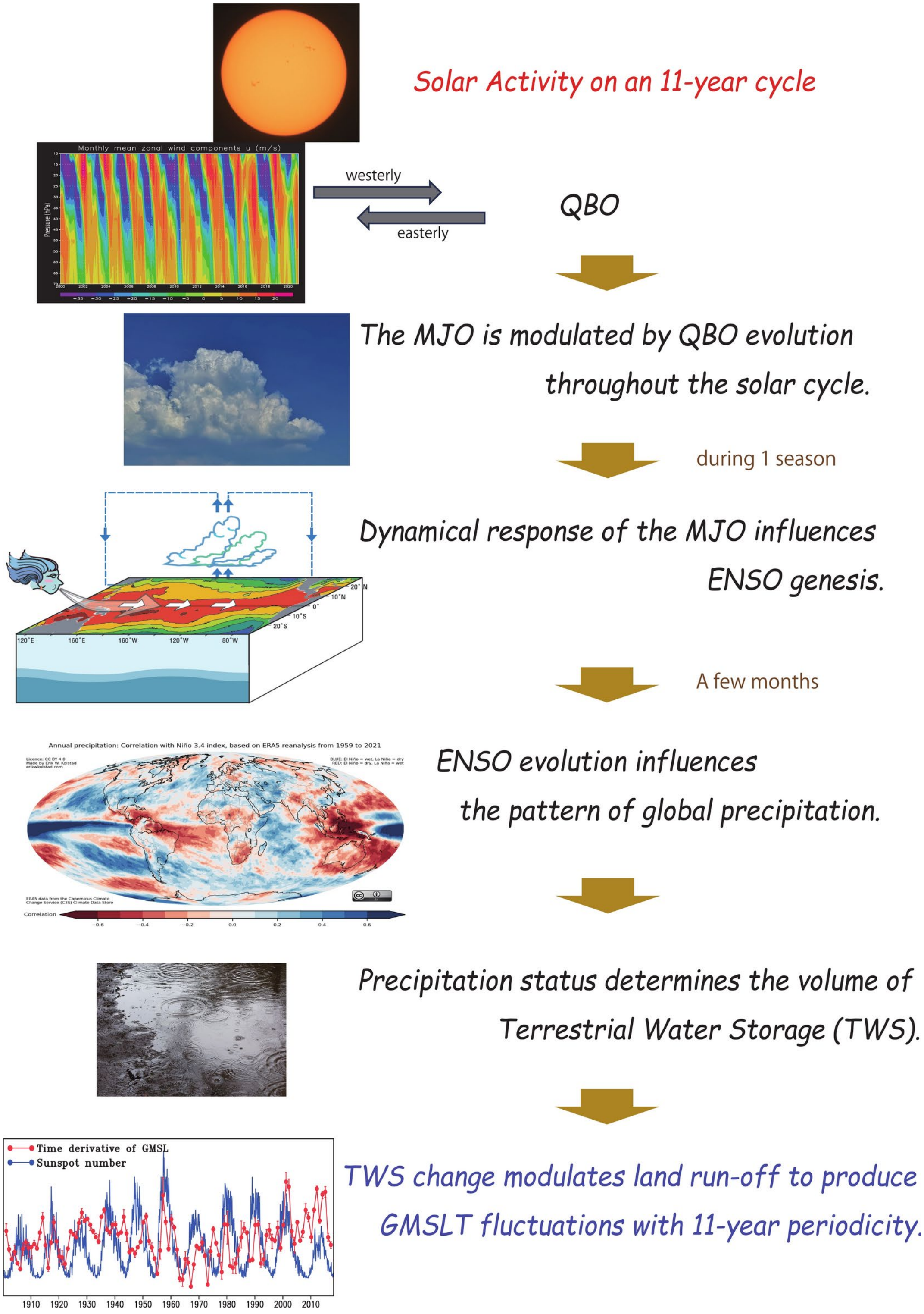

Fig. 7. Schematic view of the complete cycle of interactions determining the solar-cyclic imprint on global sea level change. The global map in relation to ENSO evolution can be found at https://erikwkolstad.com/2022/09/08/enso-precipitation-maps/

Data availability

All data used in this study can be obtained from links given in the manuscript or in the supplementary materials [see "Materials and Methods"]. The GMSL data analysed during the current study is available at https://zenodo.org/record/3862995#.YVQogDHP2Ul. The Sunspot Number data are available in WDC-SILSO, Royal Observatory of Belgium, Brussels, https://www.sidc.be/SILSO/DATA/SN_d_tot_V2.0.txt. The PDSI data is available for Dai, A. 2011, Global Monthly Dai Palmer Drought Severity Index (PDSI) in the THREDDS Data Server, psl.noaa.gov/thredds/catalog/Datasets/dai_pdsi/catalog.html. Galactic cosmic ray data is available in the Sodankyla Geophysical Observatory repository, https://cosmicrays.oulu.fi/readme.html. Altimeter data is available in the HDR GSFC. 2021. Global Mean Sea Level Trend from Integrated Multi-Mission Ocean Altimeters TOPEX/Poseidon, Jason-1, OSTM/Jason-2, and Jason-3 Version 5.1. Ver. 5.1 PO.DAAC, CA, USA., https://doi.org/https://doi.org/10.5067/GMSLM-TJ151. Terrestrial water storage datasets are available at https://figshare.com/articles/dataset/GRACE-REC_A_reconstruction_of_climate-driven_water_storage_changes_over_the_last_century/7670849. The monthly_grids_ensemble_JPL_ERA5_1979_201907. Sea surface temperature data in the NINO3.4 region is available in the NOAA repository, compiled from NOAA ERSSTv5 data, https://www.esrl.noaa.gov/psd/data/gridded/data.noaa.ersst.v5.html. Data table generated by Brian McNoldy, University of Miami (bmcnoldy@rsmas.miami.edu) was used. QBO data is available at https://www.geo.fu-berlin.de/met/ag/strat/produkte/qbo/qbo.dat. All data used in this study can be obtained from links given in the manuscript or in the supplementary materials [see "Materials and Methods"].

Received: 21 December 2024; Accepted: 23 April 2025
Published online: 16 May 2025

References:

1. Factsheet: People and Oceans, United Nations, New York; 2007 [cited 2022 Jan 18]. https://www.un.org/sustainabledevelopment/wp-content/uploads/2017/05/Ocean-fact-sheet-package.pdf.
2. Woodworth, P. L. et al. Towards reliable global allowances for sea level rise. *Glob. Planet. Change* **203**, 103522 (2021).
3. Tamisiea, M. E. et al. Sea level: Measuring the bounding surfaces of the ocean. *Philos. Trans. R. Soc. A* **372**, 20130336 (2014).
4. Boening, C. et al. The 2011 La Niña: So strong, the oceans fell. *Geophys. Res. Lett.* **39**, L19602 (2012).
5. Frederikse, T. et al. The causes of sea-level rise since 1900. *Nature* **584**, 393–397 (2020).
6. Dieng, H. B. et al. New estimate of the current rate of sea level rise from a sea level budget approach. *Geophys. Res. Lett.* **44**, 3744–3751 (2017).
7. Gulev, S.K. et al. Changing State of the Climate System. In *Climate Change 2021: The Physical Science Basis, Contribution of Working Group I to the Sixth Assessment Report of the Intergovernmental Panel on Climate Change* (Cambridge University Press, 2021).
8. Holgate, S. J. & Woodworth, P. L. Evidence for enhanced coastal sea level rise during the 1990s. *Geophys. Res. Lett.* **31**, L07305 (2004).
9. Shaviv, N. J. Using the oceans as a calorimeter to quantify the solar radiative forcing. *J. Geophys. Res.* **113**, A11101 (2008).
10. Svensmark, H. Influence of cosmic rays on earth's climate. *Phys. Rev. Lett.* **81**, 5027–5030 (1998).
11. Svensmark, H. et al. Increased ionization supports growth of aerosols into cloud condensation nuclei. *Nat. Commun.* **8**, 2199 (2017).
12. Masuda, S. et al. Simulated rapid warming of abyssal North Pacific waters. *Science* **329**, 319–322 (2010).
13. Palmer, W.C. *Meteorological Drought, Office of Climatology Research Paper*, Vol. 45 (Washington, D.C., 1965).
14. Humphrey, V. & Gudmundsson, L. GRACE-REC: A reconstruction of climate-driven water storage changes over the last century. *Earth Syst. Sci. Data* **11**, 1153–1170 (2019).
15. Humphrey, V. et al. A global recon-struction of climate-driven subdecadal water storage variability. *Geophys. Res. Lett.* **44**, 2300–2309 (2017).
16. Dai, A. & Wigley, T. M. L. Global patterns of ENSO-induced precipitation. *Geophys. Res. Lett.* **27**, 1283–1286 (2000).
17. Dai, A. et al. A global dataset of palmer drought severity index for 1870–2002: Relationship with soil moisture and effects of surface warming. *J. Hydrometeor.* **5**, 1117–1130 (2004).
18. Oki, T. & Kanae, S. Global hydrological cycles and world water resources. *Science* **313**, 1068–1072 (2006).
19. Antico, A. & Torres, M. E. Evidence of a decadal solar signal in the Amazon River: 1903 to 2013. *Geophys. Res. Lett.* **42**, 10782–10787 (2015).
20. Baker, J. C. A. et al. Questioning the influence of sunspots on Amazon hydrology: Even a broken clock tells the right time twice a day. *Geophys. Res. Lett.* **45**, 1419–1422 (2018).
21. Antico, A. & Torres, M. E. A note on the recent use of tree-ring data to investigate a Sun-Amazon River link. *J. Hydro.* **583**, 124623 (2020).
22. Labitzke, K. & van Loon, K. H. Association between the 11-year solar cycle, the QBO, and the atmosphere, I The troposphere and stratosphere on the northern hemisphere winter. *J. Atmos. Terr. Phys.* **50**, 197–206 (1998).
23. Mohanakhmar, K. Effects of solar activity and stratospheric QBO on tropical monsoon rainfall. *J. Geomag. Geoelec.* **48**, 343–352 (1996).
24. Kuroda, Y. Effect of QBO and ENSO on the solar cycle modulation of winter North Atlantic Oscillation. *J. Meteo. Soc. Jpn.* **85**, 889–898 (2007).
25. Lin, Y.-F. et al. The footprint of the 11-year solar cycle in Northeastern pacific SSTs and its influence on the Central Pacific El Niño. *Geophys. Res. Lett.* **48**, e2020GL091369 (2021).
26. Hood, L. L. et al. QBO/Solar influences on the tropical Madden–Julian oscillation: A mechanism based on extratropical wave forcing in late fall and early winter. *J. Geophys. Res.* **128**, e20222JD037824 (2023).
27. Hartten, L. M. Synoptic settings of westerly wind bursts. *J. Geophys. Res.* **101**, 16997–17019 (1996).
28. Takayabu, Y. N. et al. Abrupt termination of the 1997–98 El Niño in response to a Madden–Julian oscillation. *Nature* **402**, 279–282 (1999).
29. Bergman, J. W. et al. Intraseasonal air–sea interactions at the onset of El Niño. *J. Climate* **14**, 1702–1719 (2001).
30. Miyakawa, T. et al. A Madden–Julian Oscillation event remotely accelerates ocean upwelling to abruptly terminate the 1997/1998 super El Niño. *Geophys. Res. Lett.* **44**, 9489–9495 (2017).
31. van Loon, H. et al. Coupled air-sea response to solar forcing in the Pacific region during northern winter. *J. Geophys. Res.* **112**, D02108 (2007).
32. Martínez-Asensio, A. et al. Decadal variability of European sea level extremes in relation to the solar activity. *Geophys. Res. Lett.* **43**, 11744–11750 (2016).
33. Valle-Levinson, A. & Martin, J. B. Solar activity and lunar precessions influence extreme sea-level variability in the U.S. Atlantic and Gulf of Mexico Coasts. *Geophys. Res. Lett.* **47**, e2020GL090024 (2020).

Acknowledgements

We acknowledge the work of a number of solar- and geoscience-data providers listed in "Materials and Methods". In particular, we are indebted to Dr. V. Humphrey for the free provision of terrestrial water-storage data and instructions on their manipulation. Our work benefitted from discussions with Prof. P. Woodworth and Dr.

Mikiko Fujita. Analytical calculations and data assimilations were performed on the Earth Simulator and Data Analysis system of JAMSTEC.

Author contributions
S.M. coordinated coauthor contributions; performed analyses, developed interpretations and wrote the paper. Contributions to both the writing and interpretation came from J.P.M. while Y.A.Y. contributed to the interpretation.

Funding
This work was supported by a Japan Society for the Promotion of Science KAKENHI Grant JP22H05207.

Declarations

Competing interests
The authors declare no competing interests.

Additional information
Supplementary Information The online version contains supplementary material available at https://doi.org/10.1038/s41598-025-99880-2.

Correspondence and requests for materials should be addressed to S.M.

Reprints and permissions information is available at www.nature.com/reprints.

Publisher's note Springer Nature remains neutral with regard to jurisdictional claims in published maps and institutional affiliations.